Supplementary Information

Table of Contents

1. White Light Interferometry

The roughness of the slip surfaces has been measured using White Light Interferometer (WLI) micro-imaging. Three different and complementary devices were used; two instruments manufactured by Zygo© (the ZeScope and the Zygo NewView7300) and one instrument manufactured by Veeco© (the Wyko 2000). For all of these devices, a Michelson interferometer is coupled to a microscope with a broad-band white or green light source. A reference arm creates interference fringes with maximum intensity at equal optical path lengths of the imaging beam and reference beam. By vertical movement of the fault sample and simultaneous image capturing of the interference, we determine the maximum intensity envelope and thereby the relative height of the imaged surface at each pixel with a height resolution ~1-0.1 nm. The horizontal resolution depends on the objective lens used. With the highest magnification, the resolution is at the diffraction limit of white or green light, i.e., ~0.5 μm. In the present study, several height images for each slip surfaces have been obtained with different objective lenses. Objective lenses with a large field of view but a relatively low horizontal resolution were used to image large-scale roughness features. In contrast, small-scale roughness features were imaged using objectives lenses with a small field of view but high horizontal resolution. With the devices from Zygo© we were able to stitch multiple high-resolution small-scale individual height images to acquire large-scale topographic maps with a high spatial resolution. This last method is particularly

powerful to image a selected area of the slip surfaces over a large range of length scales and in spatial continuity. Ultimately we obtain for each surface a single power spectrum covering the full range of scales.

2. Fourier Spectral Analysis

The spectral analysis is similar to previous procedures reported in Candela et al. (2012). The original 3-D (X, Y, Z) topographic maps acquired by White Light Interferometry are first processed to remove the planar tilt of the surface and fill missing data (~10%) with linear interpolation. The data obtained are topographic maps where the Z direction was approximately perpendicular to the mean fault plane (X, Y).

From each topographic map, thousands to tens of thousands of profiles are extracted in both the slip-parallel and the slip-perpendicular direction. The four steps in the procedure to compute the spectrum of each profile are as follows: (1) Any residual drifts are removed by subtracting the best-fit trend. (2) A 3% cosine taper is applied. (3) The discrete Fourier transform is calculated, and the power spectrum is equal to the square of the amplitudes of the coefficients. (4) The power spectrum is normalized by the profile length to obtain the power spectral density. For each direction (either the slip-parallel or slip-perpendicular direction), the mean Fourier spectrum of each topographic map is then computed by averaging the spectra of the profiles.

We confirm that the noise level of the instrumental system is much lower than the measurements of fault surfaces in spectral space. We scanned a flat surface of silicon carbide produced by the Zygo as a reference surface and compared the measured spectra

to that of a typical fault surface (Figure DR1). The instrumental noise is six orders of magnitude below the fault sample.

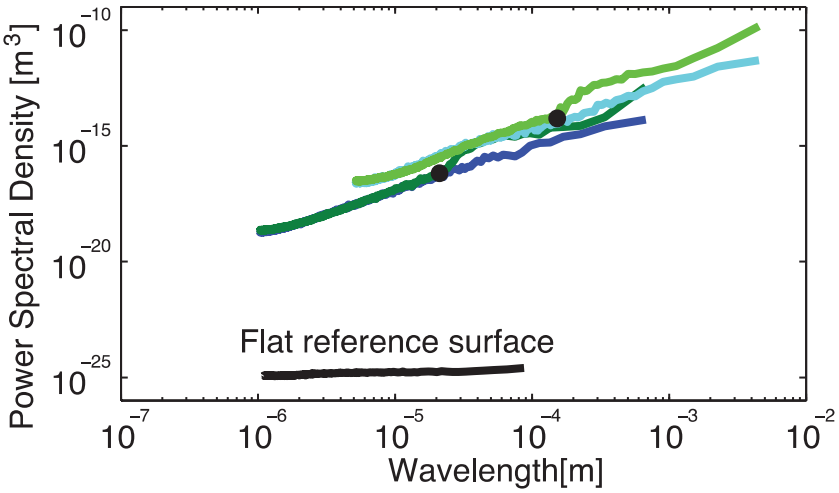

Figure DR1. Power spectral density for a flat reference surface of silicon carbide illustrates the noise level of the instrument is below the measurements of faults. The representative fault data is the same as in Figure 2c (Mount St. Helens fault) with the same symbols and colors.

Each linear portion of the spectra on the log-log graph can be fitted by a power law trend of the form $p(\lambda) = C\,(\lambda)^{1+2\zeta}$ where C is a constant prefactor, ζ is known as the Hurst exponent or roughness exponent, and λ is the wavelength. Mean spectra from LiDAR field measurements can be fit by two separate power law trends: one in the slip-parallel direction with a Hurst exponent $\zeta=0.6$ and one in the slip-perpendicular direction with a Hurst exponent $\zeta=0.8$. This feature demonstrates the continuous scale-dependent behavior of the slip surface roughness at the LiDAR scale. In fact, this behavior can be extended to

the White Light Interferometry scale, since the large wavelength end of the spectra obtained from the White Light Interferometer topographic maps can be fitted by the same power law trends in the slip-parallel and slip-perpendicular directions.

Two separate methods were used to determine the minimum grooving scale, which is defined in the main text as the scale where the mean Fourier spectra in the slip-parallel and slip-perpendicular direction coincide.

The first method consists of fitting with a linear trend the part of the spectra that visually coincide and then separately fitting the slip-perpendicular spectrum in the anisotropic regime (Fig. DR2). The crossover between the fits is the minimum grooving scale. We note in passing that the Hurst exponents of the isotropic regime range were between 0.4 and 0.6 and future work may focus the scaling properties of the newly established isotropic regime.

The second method consists in computing the normalized difference between the power spectral estimates in the slip-perpendicular and slip-parallel direction (Fig. DR2) that is:

$\Delta p = (p_{perp} - p_{para})/p_{perp.}$

The minimum grooving scale is measured as the wavelength where $\Delta p=0.3$. In other words, the isotropic regime appears when the magnitude of the power spectral density in the slip-parallel direction is at least 70% of the magnitude of the power spectral density in the slip-perpendicular direction. This particular threshold is governed by the resolution limit of the power spectra.

These two methods for picking the minimum grooving scale give identical results and the second one allows us to avoid biases inherent to human interpretation in the visual inspection of the spectra.

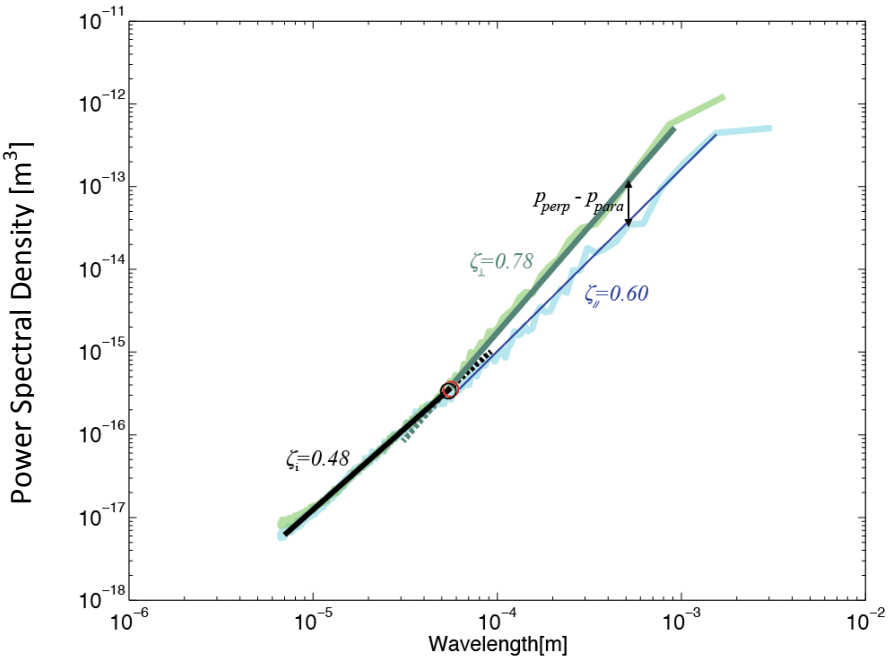

Supplementary Figure DR2. Determination of the minimum grooving scale from the Fourier analysis. Both the "fitting method" (black circle) and the "normalized difference method" (red circle) give indistinguishable minimum grooving scale results. For this representative example of one topographic map of the Mount St. Helens fault, the Hurst exponents in the slip-parallel, slip-perpendicular direction, and isotropic regime are 0.60, 0.78 and 0.48, respectively.

3. Calculation of Average Asperity Height and Aspect Ratio

The average asperity height H can be linked to the power spectral density by using Parseval's theorem. The result is:

$$H = \left(\int_{1/L}^{\infty} p(k)dk\right)^{1/2} \quad \text{(A1)}$$

where L is the asperity scale (maximum wavelength) and $k = 1/\lambda$ where λ is the wavelength (Brodsky et al., 2011). Now combining $p(\lambda) = C(\lambda)^{1+2\zeta}$ with eq. *A1*, it follows $H = [C/(2\zeta)]^{0.5}L^{\zeta}$. Consequently, for a self-similar fractal surface $\zeta=1$, the roughness aspect ratio H/L is constant and equal to $[C/2]^{0.5}$. We used this relationship to compute the red lines of constant roughness aspect ratio that are used in Figs. 2-3 for comparison to the data.

4. Connection Between Aspect Ratio, Shear Strain and Yielding

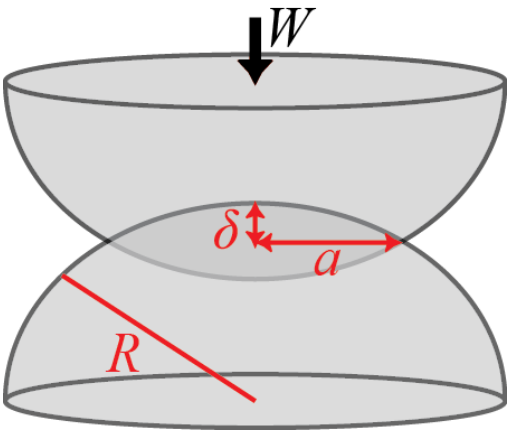

Supplementary Figure DR3. Hertzian contact between two elastic deformable spheres.

When squeezing two rough slip surfaces, a simple asperity contact model is the collision between two identical spheres (Fig. DR3). For this model, we can apply Hertzian contact theory to calculate the resulting stress field from the deformation of elastic spheres as

originally solved by Hertz in 1881 (Hertz, 1881). In this model, the flattened portion of the asperity's aspect ratio is δ/a in Fig. DR3. The resulting shear strain is proportional to this aspect ratio, which is the single asperity equivalent of H/L (Kirkpatrick and Brodsky, 2014; Brodsky et al., 2016).

The Hertz solution is strictly applicable only at small strains. However, for more general geometries, similar results apply. For a Gaussian distribution of summit heights, the solution for the mean normal stress as a function of the aspect ratio is

$$\sigma = (E'/\sqrt{2})\ (\delta/L) \qquad (A2)$$

where $E' = 2(1-\nu^2/E)^{-1}$, E is the Young's modulus, ν is the Poisson ratio, and σ is the mean normal stress (Mikic, 1974). Interestingly, for elastic self-affine rough surfaces, the same scaling between normal stress, strain and aspect ratio can be derived (Batrouni et al., 2002). A numerical solution shows that for the fully elastic squeeze of self-affine surfaces is

$$\sigma = (1/\kappa)\ E'(\delta/L) \qquad (A3)$$

where κ a dimensionless constant close to 2 (Hyun et al., 2004).

It remains to predict the conditions that should lead to the initiation of plastic deformation for two facing rough self-affine surfaces. Plasticity is defined as a rheology with a yield stress. Assuming the mean normal stress at the plastic yield stress of the material σ_y and substituting $\sigma_y = \mathcal{H}/3$ (Mikic, 1974), from eq. *A3* the condition for the onset of plasticity is

$$(H/L)_c \sim 2/3\ \mathcal{H}/E' \qquad (A4).$$

5. Fault Descriptions

Below we document the samples and localities used for analysis. In the figure accompanying each fault description, we show: (1) a representative topographic map measured using a White Light Interferometer, (2) the spectra of 2-4 representative samples along with their corresponding minimum grooving scales and (3) the remaining minimum grooving scales measured on the full dataset.

Since this paper suggests plastic failure at small scales, we include in the fault description evidence of plastic deformation where it was observed. All faults also include brittle features at large scales such as fractures, toolmarks and cataclasis. Since brittle deformation is a well-established feature of fault slip, we do not specifically enumerate the brittle structures for each fault here.

5.1. Natural Slip Surfaces

5.1.1. Corona Heights

The Corona Heights oblique strike-slip fault, located in the Castro district of San Francisco, crosscuts brown Franciscan cherts and was exposed by a quarry built after the 1906 earthquake. The relatively recent exposure and the high resistance of cherts to weathering allows for excellent preservation of the slip surfaces. Based on the lack of observed offsets at the boundary of the chert body, the total slip accumulated is estimated to be less than 50 m (Kirkpatrick and Brodsky, 2014). The slip surfaces studied are both reflective mirrors and marked by multi-scale striations (Fig. DR4). The slip surfaces are coated by a thin layer of 100 nm to 1μm grains of quartz interpreted as a relict of silica gel (Kirkpatrick et al.,

2013). This peculiar texture might have favored the dynamic weakening of the fault during past earthquakes. Under the slip surfaces bands of preferred crystallographic orientation are common and are evidence of plastic deformation and/or stress-driven diffusive mass transfer (Kirkpatrick et al., 2013).

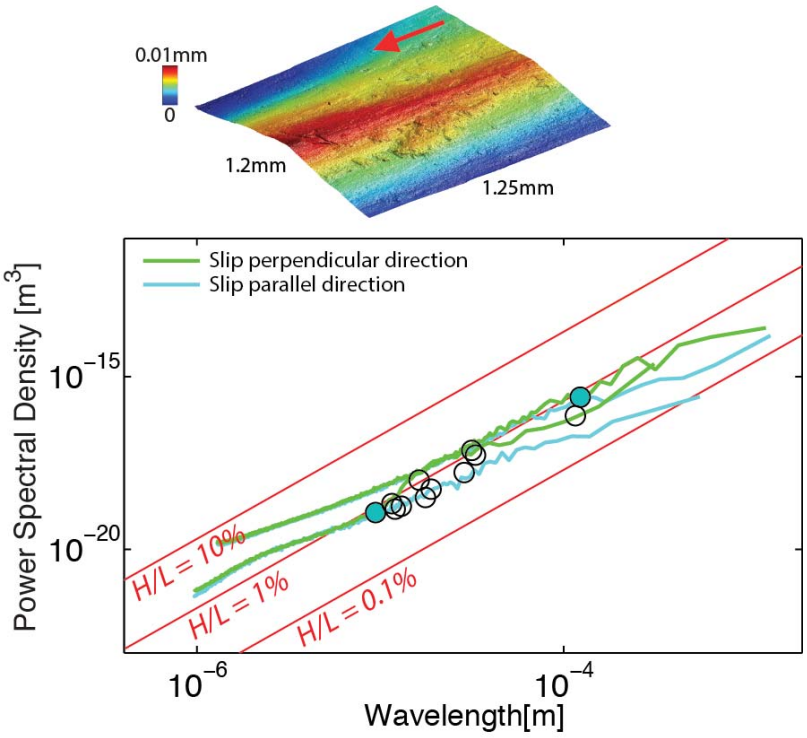

Supplementary Figure DR4. Fourier spectra and minimum grooving scales for the Corona Heights fault. We analyzed 12 topographic maps like the example at the top. The spectra of two representative samples are shown and their respective minimum grooving scales are filled circles. Empty circles show the minimum grooving scales of the 10 remaining topographic maps.

5.1.2. Flowers Pit

Flowers Pit fault is a part of the Klamath graben faults system in the northwestern Basin and Range (Sagy and Brodsky, 2009). The locally mirror-like and striated fault surfaces (Fig. DR5) have been exposed by recent quarrying, and thus are relatively unweathered. The range of accumulated displacement along the slip surfaces was estimated to be between 100 m to 300 m (Brodsky et al., 2011). Microstructural observations of the slip surfaces revealed fluidization and ductile deformation (Sagy and Brodsky, 2009). Branches of micro-hydrofractures adjacent to the slip surfaces were interpreted as evidence of internal pressurization during the rapid slip of an earthquake.

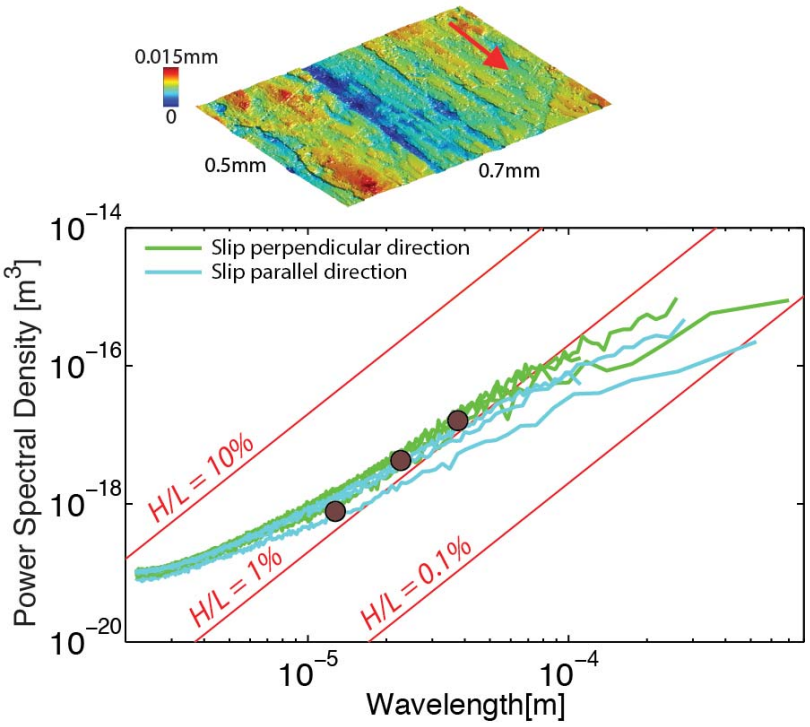

Supplementary Figure DR5. Fourier spectra and minimum grooving scales for the Flowers pit fault. We analyzed 3 topographic maps like the example at the top. The

spectra of all three samples are shown and their respective minimum grooving scales are filled circles.

5.1.3. Mount St. Helens

The 2004-2008 eruption of Mount St. Helens extruded dacite spines. The sliding surface between spine 7 and the crater wall formed a fault. The frictional sliding between the spine and the crater wall was associated with a series of regular stick-slip earthquakes (Iverson et al., 2006). We analyzed samples of this fault that were collected in 2008 to ensure minimal weathering (Fig. DR6). Textural evidence indicates that crystallization and solidification of the ascending magma preceded the slip surface formation (Cashman et al., 2008). The slip surfaces are striated but are not reflective mirrors. The total slip accumulated along the dacite fault surface is probably less than 500 m and its mineralogy is dominated by plagioclase, hypersthene and amphibole (Cashman et al., 2008).

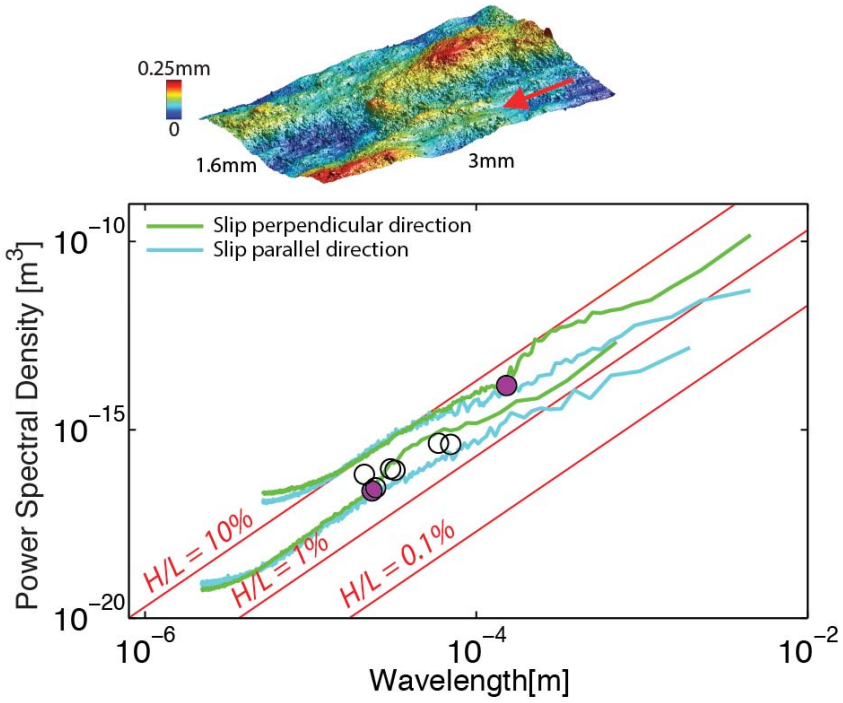

Supplementary Figure DR6. Fourier spectra and minimum grooving scales for the Mount St. Helens fault. We analyzed 8 topographic maps like the example at the top. The spectra of two representative samples are shown and their respective minimum grooving scales are filled circles. Empty circles show the minimum grooving scales of the six remaining topographic maps.

5.1.4. Bolu

The Bolu fault is part of the North Anatolian strike-slip fault system in Turkey. The studied slip surfaces offset limestone and are part of the section that ruptured during the 1944 earthquake (Candela et al., 2012). From paleo-seismological constraints, the lower bound

of the slip accumulated along the studied slip surfaces is 20 m. The slip surfaces are striated but are not reflective mirrors (Fig. DR7). They are in a fine-grained layer of less than 1 mm of thickness and often truncate large clasts.

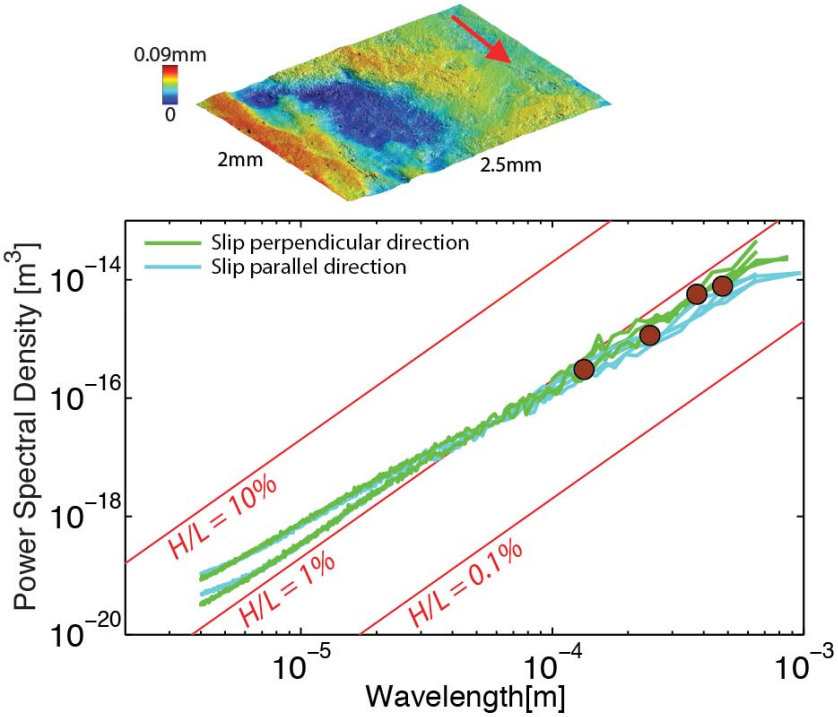

Supplementary Figure DR7. Fourier spectra and minimum grooving scales for the Bolu fault. We analyzed 4 topographic maps like the example at the top. The spectra of all samples are shown and their respective minimum grooving scales are filled circles.

5.1.5. SDZ-G28

The studied slip surfaces (Fig. DR8) are from the main borehole of the San Andreas Fault Observatory at Depth (SAFOD) project designed to drill through the creeping section of the

San Andreas Fault Zone (Hadizadeh et al., 2012; Moore, 2014). The studied sample (G28 - 3197.24m MD) is from the Southwestern Deforming Zone (SDZ). It has a scaly texture with pervasive shiny and striated slip surfaces in Mg-rich swelling clays (saponite and corrensite) separating lenses of serpentinite porphyroclasts and lithic (Hadizadeh et al., 2012; Moore, 2014). Pervasive stress-driven diffusive mass transfer at the grain boundaries is observed and might contribute to aseismic creep (Hadizadeh et al., 2012).

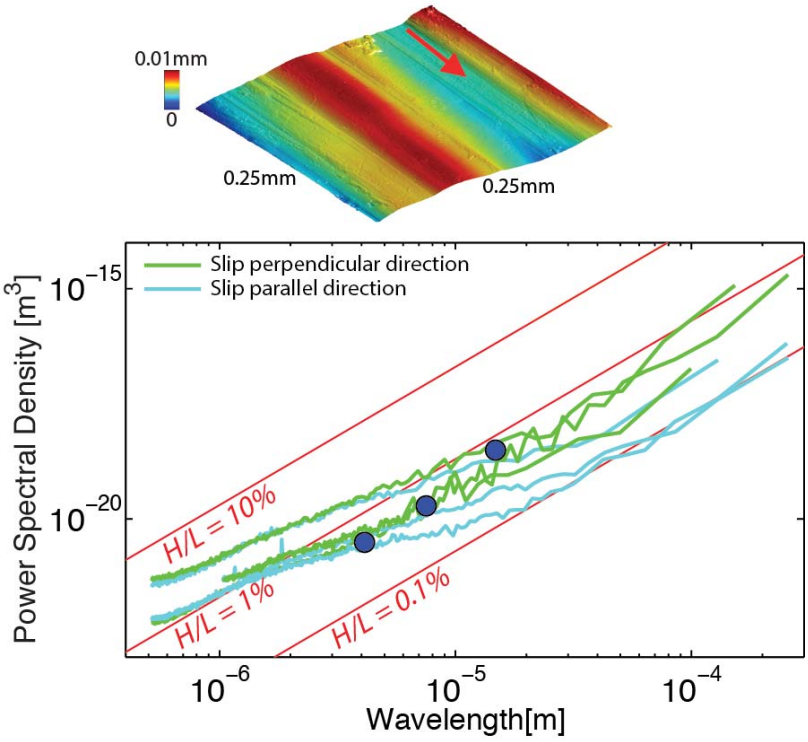

Supplementary Figure DR8. Fourier spectra and minimum grooving scales for the SDZ-G28 fault. We analyzed 3 topographic maps like the example at the top. The spectra of all three samples are shown and their respective minimum grooving scales are filled circles.

5.1.6. Dixie Valley

The Dixie Valley normal fault is a part of the Basin and Range province in Nevada. Major historical earthquakes occurred in the region of the studied slip surfaces (Power and Tullis, 1989). Geological and mineralogical constraints indicate that the both shiny and striated slip surfaces (Fig. DR9) formed at depths of less than 2 km (Power and Tullis, 1989). The total displacement accumulated along the fault zone might be as large as 3-6 km but the slip on each individual slip surface might be as small as 10 m (Candela et al., 2012). The slip surfaces are characterized by single crystals of quartz or fragments up to 200 microns in size surrounded by an ultra-fine matrix composed of hydrothermal quartz. This has resulted in extremely good preservation of the slip surfaces. As was observed for the Corona Heights fault, under the slip surfaces, bands of preferred crystallographic orientation are common and provide evidence of plastic deformation and/or stress-driven diffusive mass transfer (Power and Tullis, 1989; Candela and Renard, 2012). Power and Tullis (1989) suggested that the interplay between this continuous plastic deformation and brittle fracturing might be the cause of the fine-grained mirror-like aspect of the slip surfaces.

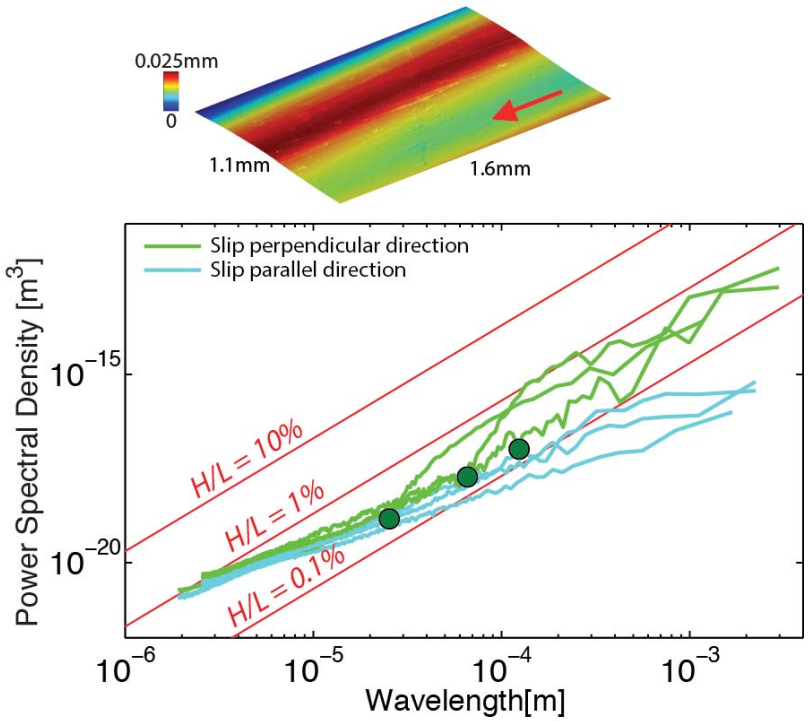

Supplementary Figure DR9. Fourier spectra and minimum grooving scales for the Dixie Valley fault. We analyzed 3 topographic maps like the example at the top. The spectra of all three samples are shown and their respective minimum grooving scales are filled circles.

5.1.7. Simi Valley

The studied slip surfaces (Fig. DR10) are part of a small-displacement normal fault crosscutting sandstone in the Santa Susana Field Laboratory (Cilona et al., 2014). The slip

surfaces have grooves and striations but are not shiny. The exposed surface is <10 m and is not on a regionally significant fault.

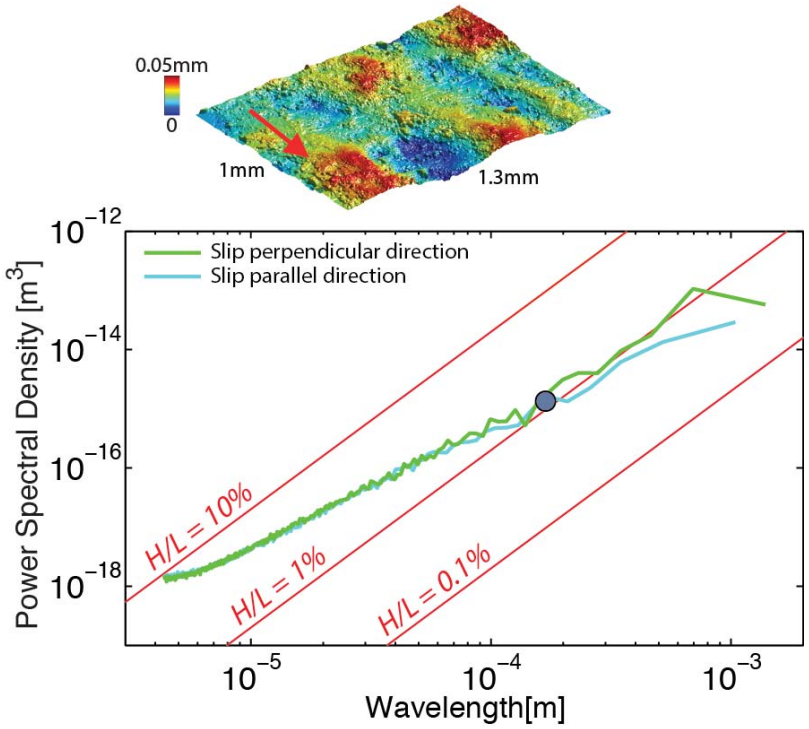

Supplementary Figure DR10. Fourier spectra and minimum grooving scale for the Simi Valley fault. Spectra and minimum grooving scale (filled circle) of the topographic map at top.

5.1.8. Foiana line

The Foiana Line is a sinistral transpressive fault zone in the Italian Southern Alps that crosscuts dolostones and is exhumed from 1-2.5 km depth (Fondriest et al., 2013). The cumulative displacement on each studied slip surface can be as small as 0.04 m. The

studied slip surfaces are both shiny and striated (Fig. DR11). They are in a compact and ultrafine-grained layer of extreme localization (<20 microns). The surfaces often truncate large clasts. Based on comparison with experiments (see dolomite gouge experiments), the mirror-like aspect of the slip surfaces has been interpreted as a signature of seismic faulting (Fondriest et al., 2013).

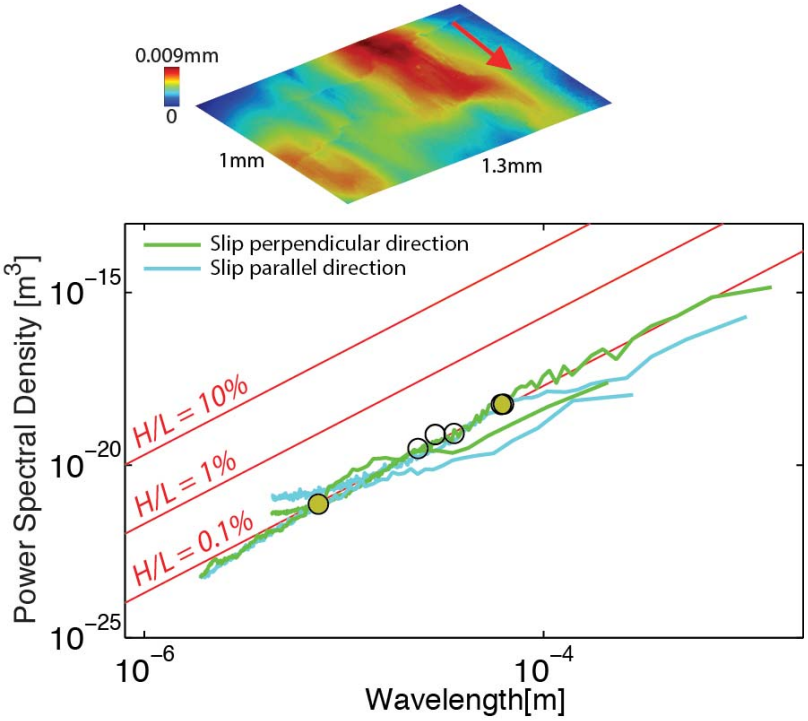

Supplementary Figure DR11. Fourier spectra and minimum grooving scales for the Foiana line fault. We analyzed 7 topographic maps like the example at the top. The spectra of two representative samples are shown and their respective minimum grooving scales are filled circles. Empty circles show the minimum grooving scales of the five remaining topographic maps.

5.2. Experimental Slip Surfaces

5.2.1. Granite Bare Surfaces

The scanned slip surfaces are from a triaxial frictional sliding experiment performed and reported by Goebel et al. (2013) with a saw-cut surface. Prior to the experiment, the saw-cut surface was ground using silicon-carbide abrasives with a range of grain sizes from 16.5 to 59 μm. Three stick-slip events where recorded during this experiment. A constant confining pressure of 120 MPa was maintained and the estimated normal stress resolved along the fault surface was 234 MPa. The post-experiment fault surface (Fig. DR12) was decorated with striations that might be associated with individual stick-slip events as proposed by Engelder and Scholz (1976).

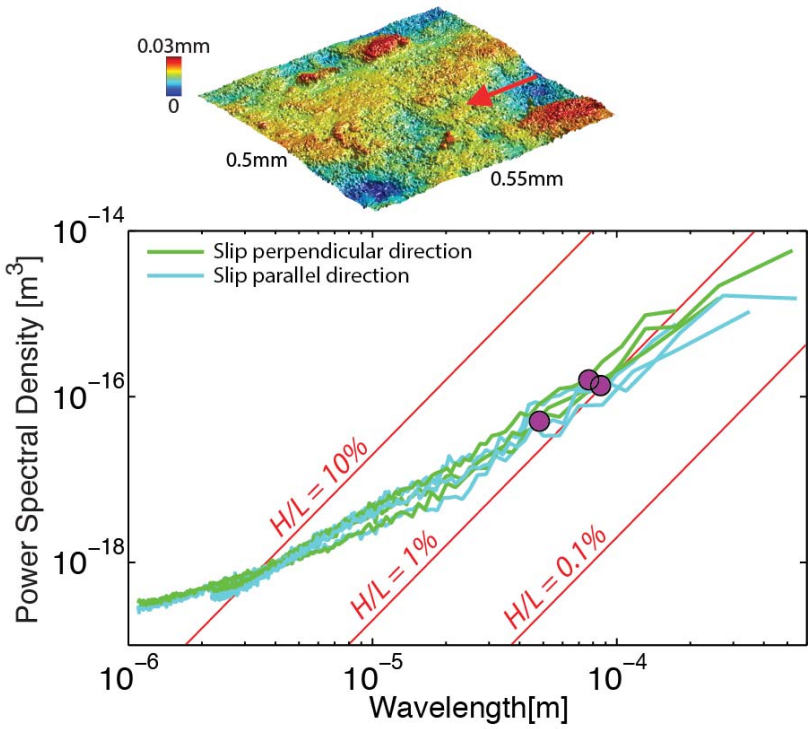

Supplementary Figure DR12. Fourier spectra and minimum grooving scales for the granite bare surfaces experiments. We analyzed 3 topographic maps like the example at the top. The spectra of all three samples are shown and their respective minimum grooving scales are filled circles.

5.2.2. SDZ-G28 and Antigorite Gouge

The studied slip surfaces (Fig. DR13a) are from two gouge samples deformed during triaxial velocity stepping experiments that slid at 0.001 to 10 μm/s with a temperature of 250°C and an effective normal stress of 100 MPa performed and reported by Moore et al. (2012). One sample is the reconstituted, Mg-clay-rich SDZ-G28 gouge of the SAFOD project

(see SDZ-G28), and the other sample is a pure antigorite serpentinite gouge. The pure antigorite gouge is much stronger (higher overall frictional strength). However, both samples are prone to slip aseismically as revealed by their velocity strengthening behavior in response to velocity steps (Moore et al., 2012) (Fig. DR13b). We determined values of D_c and other constitutive parameters by fitting the data to the Dieterich form of the rate-state constitutive law for friction (Dieterich, 1979; Reinen and Weeks, 1993; Blanpied et al., 1998):

$$\mu = \mu_0 + a\ln(V/V_0) + b\ln(V_0\Theta/D_c) \quad \text{(A5)}$$

and

$$d\Theta/dt = 1 - (V\Theta/D_c), \quad \text{(A6)}$$

where a and b are the empirically derived constants (dimensionless); Θ the state variable (unit of time); and D_c the critical slip distance. The data indicate a one-state variable behavior and the fits of each individual velocity step were not significantly improved using the Dieterich equations with two-state variables. The value of D_c is slightly larger for the antigorite gouge (D_c = 69 +/- 22 μm) compared to the SDZ-G28 gouge (D_c = 19 +/- 8 μm) (Fig. DR13b, Table DR1). Interestingly the roughness measurements capture this trend, that is, L_c is slightly larger for the antigorite gouge ($L_c \sim$ 15-30 μm) compared to the SDZ-G28 gouge ($L_c \sim$ 4-7 μm) (Fig. DR13a).

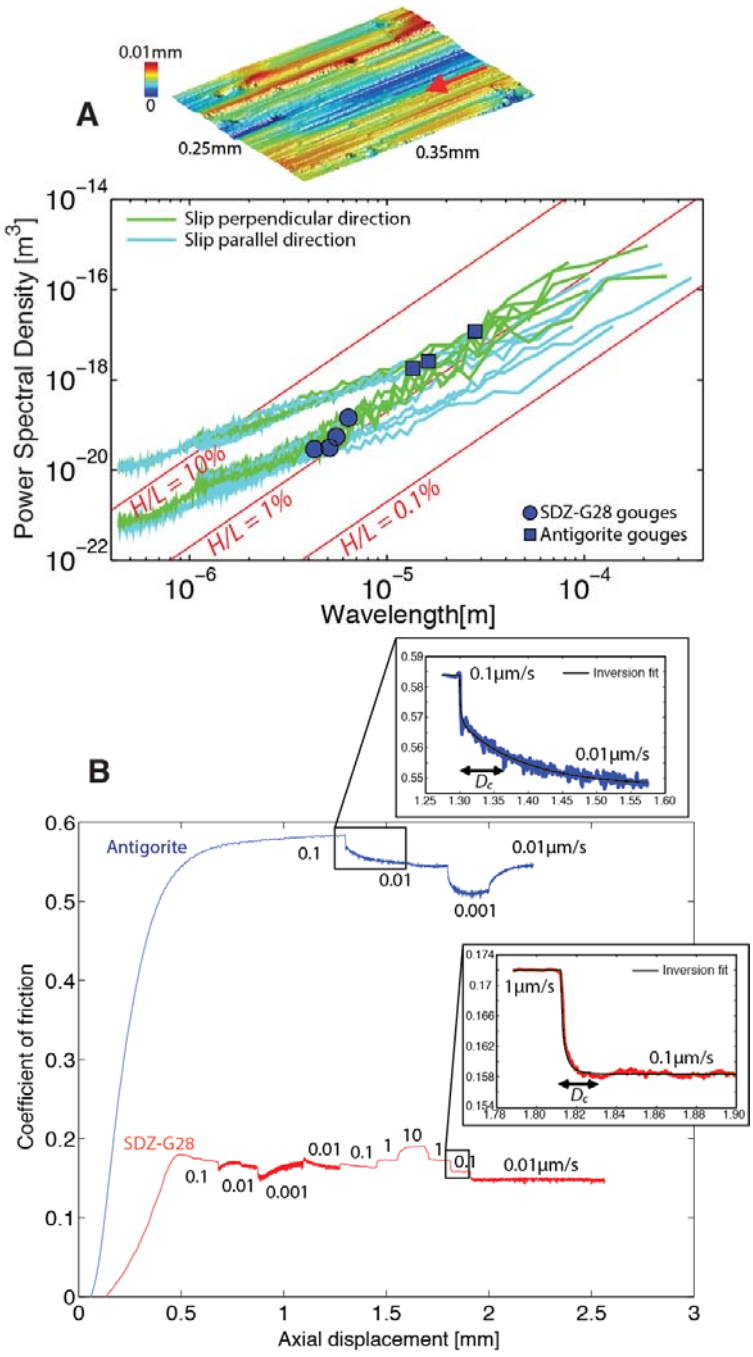

Supplementary Figure DR13. A: Fourier spectra and minimum grooving scales for the SDZ-G28 and antigorite gouge experiments. Spectra and minimum grooving scales (filled

circles and squares) of the seven analyzed topographic maps (one example at the top) are displayed. B: Friction data during velocity steps for the SDZ-G28 and antigorite gouges.

Supplementary Table DR1. Values of D_c for all velocity steps of SDZ-G28 and antigorite gouges. The range of velocities indicate the starting and stopping velocity for each step. The standard error in D_c is less than 15% for each individual velocity step.

	Velocity steps (μm/s)	D_c (μm)
Antigorite	0.1-0.01	95
	0.01-0.001	56
	0.001-0.01	57
SDZ-G28	0.1-0.01	20
	0.01-0.001	34
	0.001-0.01	20
	0.01-0.1	26
	0.1-1	13
	1-10	16
	10-1	22
	1-0.1	6.0
	0.1-0.01	11

5.2.3. Limestone Bare Surfaces

The studied slip surfaces (Fig. DR14) are from two friction experiments performed and reported by Tisato et al. (2012) with a compression-torsion apparatus on two ring-shaped limestone samples at subseismic to seismic slip rates (340 mm/s) with normal stresses from 3 to 5 MPa. The only difference between the two experiments is the initial surface roughness of the two ring-shaped bare surfaces. After cutting the samples by water-jet, the future sliding surfaces were polished with sandpaper to impose a specific initial roughness. The sandpaper used for one sample had an average particle size of 15.3μm and for the other one the sandpaper had an average particle size of 97μm. For both experiments first a low velocity stage (50 μm/s) was used to achieve a stable (slip-independent) value for friction. After this low velocity stage, a rapid acceleration was performed to reach the target higher slip rate (340mm/s). For both experiments the initial limestone was composed of ~99% calcite with grain size <5μm. At the end of the low-velocity stage, the sliding surfaces were covered by flat, submicron grains and the initial roughness was destroyed. At the end of the high-velocity stage, the calcite with submicron grains was buried under a nanoparticle layer coating the slip surfaces. These are the striated and shiny slip surfaces that we analyzed in the White Light Interferometer.

The nanoparticles coating the slip surfaces at the end of the experiments cannot be explained by brittle fracturing comminution processes alone. In fact, according to Griffith theory, it should be extremely energy consuming to produce particles of less than 1μm in size by fracturing. The explanation proposed by Tisato et al. (2012) is that the asperities adhere due to enhanced plastic deformation because of the temperature increase at

asperity contacts and the high coupling results in fracturing and the production of nanopowders. A strong velocity weakening is observed in both experiments. By fitting the friction data with the rate and state friction equations, D_c is found to be around 100 μm for both experiments. The strong velocity weakening observed in their experiments is consistent with the activation of flash heating and powder lubrication after the destruction of the original roughness (Tisato et al., 2012). During the abrupt acceleration at the initiation of sliding, flash heating was probably the dominant weakening mechanism, and then during most of the sliding the weakening was probably dominated by powder lubrication. These conclusions reveal that plastic deformation enhanced by the temperature rise at asperity contacts is a key ingredient of the weakening in both the initial flash heating and the powder lubrication during sliding.

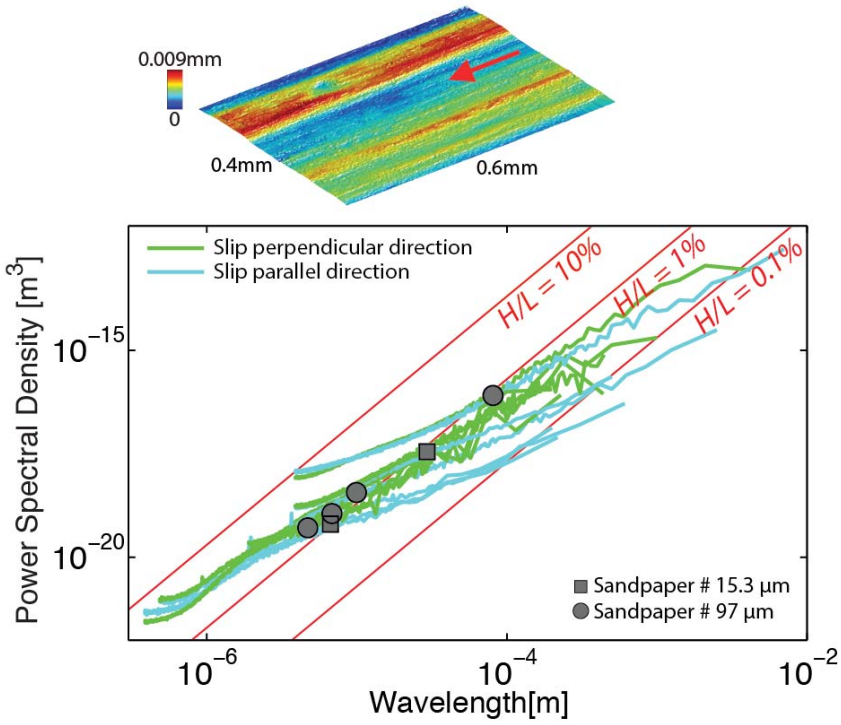

Supplementary Figure DR14. Fourier spectra and minimum grooving scales for the limestone bare surfaces experiments. Spectra and minimum grooving scales (filled symbols) of the six topographic maps (at the top one example) analyzed are displayed.

5.2.4. Dolomite Gouges

The studied slip surfaces (Fig. DR15) are from three low- to high- velocity experiments performed and reported by Fondriest et al. (2013) using a rotary-shear friction apparatus (SHIVA: Slow to High Velocity Apparatus) on dolostone gouge from the Fiona line outcrop (100% dolomite, grain size <250µm). The normal stress was set at ~26 MPa and the only parameter that was changed between the three experiments was the slip rate: 1 mm/s, 0.1 m/s, and 1 m/s. At the end of the low slip rate experiment the slip surface was only striated

and no frictional weakening was observed. In contrast, at a seismic slip rate (1 m/s), a strong frictional weakening was observed and accompanied by the creation of a mirror-like striated surface. This experimental mirror-like striated surface is similar to the ones observed for the natural slip surfaces of the Foiana line. The mirror-like striated surface consists of a compact fine-grained layer of partially welded dolostone clasts 0.1–10 μm in size and the surface truncates larger clasts as observed along the Foiana Line. Fondriest et al. (2013) proposed that at a high slip rate (1m/s) the temperature rise during frictional sliding could activate crystal plasticity and a sintering processes within the fine-grained layer.

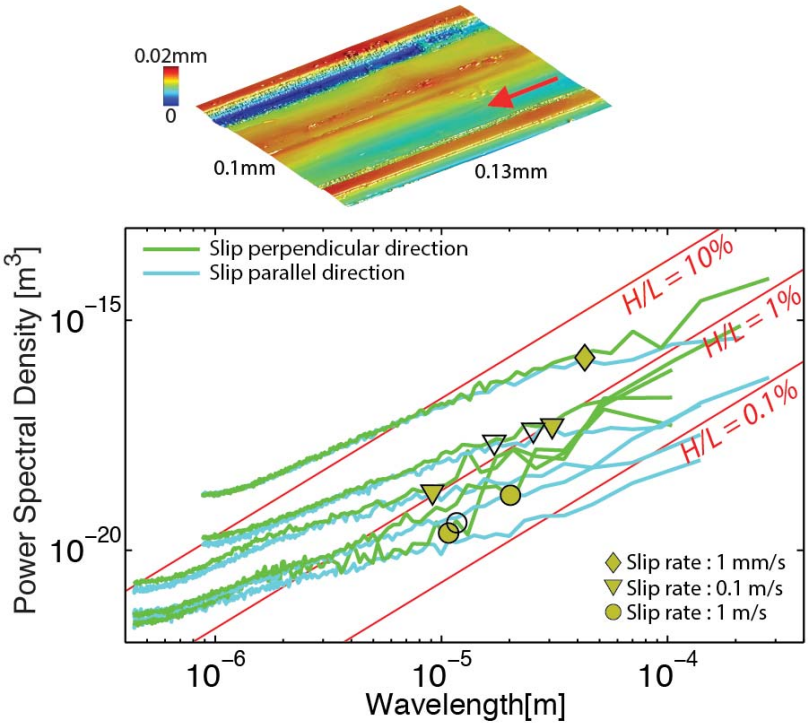

Supplementary Figure DR15. Fourier spectra and minimum grooving scales for the dolomite gouges experiments. Among the eight topographic maps analyzed (at the top one example), only the spectra of five representative topographic maps and their respective minimum grooving scales (filled circles) are displayed. Empty circles correspond to the three remaining topographic maps.

6. References

Batrouni, G.G., Hansen, A., and Schmittbuhl, J., 2002, Heterogeneous interfacial failure between two elastic blocks: Physical Review E, v. 65, no. 3, doi: 10.1103/PhysRevE.65.036126.

Blanpied, M.L., Marone, C.J., Lockner, D.A., Byerlee, J.D., and King, D.P., 1998, Quantitative measure of the variation in fault rheology due to fluid-rock interactions: Journal Of

Geophysical Research, v. 103, no. B5, p. 9691–9712, doi: 10.1029/98JB00162.

Brodsky, E.E., Gilchrist, J.J., Sagy, A., and Collettini, C., 2011, Faults smooth gradually as a function of slip: Earth and Planetary Science Letters, v. 302, no. 1, p. 185–193, doi: 10.1016/j.epsl.2010.12.010.

Brodsky, E.E., Kirkpatrick, J.D., and Candela, T., 2016, Constraints from fault roughness on the scale-dependent strength of rocks: Geology, v. 44, no. 1, p. 19–22, doi: 10.1130/g37206.1.

Candela, T., and Renard, F., 2012, Segment linkage process at the origin of slip surface roughness: Evidence from the Dixie Valley fault: Journal of Structural Geology, v. 45, p. 87–100, doi: 10.1016/j.jsg.2012.06.003.

Candela, T., Renard, F., Klinger, Y., Mair, K., Schmittbuhl, J., and Brodsky, E.E., 2012, Roughness of fault surfaces over nine decades of length scales: Journal of Geophysical Research, v. 117, p. 8409, doi: 10.1029/2011JB009041.

Cashman, K.V., Thornber, C.R., and Pallister, J.S., 2008, From dome to dust: Shallow crystallization and fragmentation of conduit magma during the 2004-2006 dome extrusion of Mount St. Helens, Washington: US Geological Survey professional paper, v. 1750, p. 387–413.

Cilona, A., Aydin, A., and Johnson, N.M., 2014, Permeability of a fault zone crosscutting a sequence of sandstones and shales and its influence on hydraulic head distribution in the Chatsworth Formation, California, USA: Hydrogeology Journal,, p. 104, doi: 10.1007/s10040-014-1206-1.

Dieterich, J.H., 1979, Modeling of rock friction: 1. Experimental results and constitutive equations: Journal of Geophysical Research, v. 84, no. B5, p. 2161–2168, doi: 10.1029/JB084iB05p02161.

Engelder, J.T., and Scholz, C.H., 1976, The role of asperity indentation and ploughing in rock friction—II: Influence of relative hardness and normal load: International Journal of Rock Mechanics and Mining Sciences, v. 13, p. 155–163.

Fondriest, M., Smith, S., Candela, T., and Nielsen, S.B., 2013, Mirror-like faults and power dissipation during earthquakes: Geology, v. 41, no. 11, p. 1175–1178, doi: 10.1130/g34641.1.

Goebel, T.H.W., Candela, T., Sammis, C.G., Becker, T.W., Dresen, G., and Schorlemmer, D., 2013, Seismic event distributions and off-fault damage during frictional sliding of saw-cut surfaces with pre-defined roughness: Geophysical Journal International,, doi: 10.1093/gji/ggt401.

Hadizadeh, J., Mittempergher, S., Gratier, J.-P., Renard, F., di Toro, G., Richard, J., and Babaie, H.A., 2012, A microstructural study of fault rocks from the SAFOD: Implications for the deformation mechanisms and strength of the creeping segment of the San Andreas Fault: Journal of Structural Geology, v. 22, p. 246–260, doi: 10.1016/j.jsg.2012.04.011.

Hertz, H., 1881, On the elastic contact of solids: J. reine angew. Math, v. 92, p. 156–171.

Hyun, S., Pei, L., Molinari, J.F., and Robbins, M.O., 2004, Finite-element analysis of contact between elastic self-affine surfaces: Physical Review E, v. 70, no. 2, doi: 10.1103/PhysRevE.70.026117.

Iverson, R.M., Dzurisin, D., Gardner, C.A., Gerlach, T.M., LaHusen, R.G., Lisowski, M., Major, J.J., Malone, S.D., Messerich, J.A., Moran, S.C., Pallister, J.S., Qamar, A.I., Schilling, S.P., and Vallance, J.W., 2006, Dynamics of seismogenic volcanic extrusion at Mount St Helens in 2004–05: Nature, v. 444, no. 7118, p. 439–443, doi: 10.1038/nature05322.

Kirkpatrick, J.D., and Brodsky, E.E., 2014, Slickenline orientations as a record of fault rock rheology: Earth and Planetary Science Letters, v. 408, p. 24–34, doi: 10.1016/j.epsl.2014.09.040.

Kirkpatrick, J.D., Rowe, C.D., White, J.C., and Brodsky, E.E., 2013, Silica gel formation during fault slip: Evidence from the rock record: Geology, v. 41, no. 9, p. 1015–1018, doi: 10.1130/G34483.1.

Mikic, B.B., 1974, Thermal contact conductance - theoretical considerations: International Journal of Heat and Mass Transfer, v. 17, no. 2, p. 205–214, doi: 10.1016/0017-9310(74)90082-9.

Moore, D.E., 2014, Comparative mineral chemistry and textures of SAFOD fault gouge and damage-zone rocks: Journal of Structural Geology, v. 68, no. PA, p. 82–96, doi: 10.1016/j.jsg.2014.09.002.

Moore, D.E., Lockner, D.A., Morrow, C.A., and Hickman, S., 2012, Frictional Strengths of SAFOD Core and Franciscan Melange Samples at Elevated Temperatures: AGU Fall Meeting Abstracts S11A-01.

Power, W.L., and Tullis, T.E., 1989, The Relationship Between Slickenside Surfaces in Fine-Grained Quartz and the Seismic Cycle: Journal of Structural Geology, v. 11, no. 7, p. 879–893, doi: 10.1016/0191-8141(89)90105-3.

Reinen, L.A., and Weeks, J.D., 1993, Determination of rock friction constitutive parameters using an iterative least squares inversion method: Journal Of Geophysical Research, v. 98, no. B9, p. 15937, doi: 10.1029/93jb00780.

Sagy, A., and Brodsky, E.E., 2009, Geometric and rheological asperities in an exposed fault zone: Journal of Geophysical Research, v. 114, no. B2, p. B02301, doi: 10.1029/2008JB005701.

Tisato, N., di Toro, G., de Rossi, N., Quaresimin, M., and Candela, T., 2012, Experimental investigation of flash weakening in limestone: Journal of Structural Geology, v. 38, p. 183–199, doi: 10.1016/j.jsg.2011.11.017.